

Relativistic Effects in LaBi_2 Thin Films

Reiley Dorrian,^{1,2} Sungmin Song,^{3,4} Jinwoong Kim,^{4,5} Mizuki Ohno,^{1,2}
Seung-Hoon Jhi,³ Nicholas Kioussis,⁴ and Joseph Falson^{1,2,*}

¹*Department of Applied Physics and Materials Science,
California Institute of Technology, Pasadena, California 91125, USA.*

²*Institute for Quantum Information and Matter,
California Institute of Technology, Pasadena, California 91125, USA.*

³*Department of Physics, Pohang University of Science
and Technology, Pohang 37673, Republic of Korea*

⁴*Department of Physics and W. M. Keck Computational Materials Theory Center,
California State University Northridge,
Northridge, California 91330, USA.*

⁵*Korea Institute for Advanced Study, Seoul 02455, Republic of Korea*

Abstract

Chemical substitution in crystalline quantum materials is a powerful way to explore the consequences of strong spin-orbit coupling on their structural and electronic properties. In this work, we present an investigation of thin films of the LaPn_2 ($Pn = \text{Sb, Bi}$) class of layered square-net intermetallics. We report the growth of LaBi_2 with a pristine layer-by-layer growth mode, classifying it as a good metal displaying superconductivity at ~ 0.55 K. Compared to LaSb_2 , we attribute the enhanced metallic behavior and improved growth dynamics of LaBi_2 to significant relativistic corrections to its electronic band structure and the resulting impact on both surface energy and intrinsic phonon scattering.

I. INTRODUCTION

Spin-orbit coupling (SOC) – the relativistic coupling of an electron’s momentum to its spin – is a mechanism of great importance for discovering and engineering novel electronic phases in crystalline materials. Under certain symmetry constraints, SOC acts to gap out spin-degenerate crossings in the electronic band structure, leading to inverted bands and symmetry-protected topological states [1, 2]. In the superconducting state, strong SOC can impart significant resilience to applied magnetic fields through both scattering processes [3] and momentum-dependent spin stiffness in the band structure, also known as Ising pairing [4], while potentially enabling unconventional pairing symmetries through the mixing of spin-singlet and -triplet components [5].

As the strength of SOC is related to the atomic mass of constituent atoms, chemical substitution in crystalline compounds is a commonly employed method for engineering the impacts of SOC [1, 2, 7]. Exploring this degree of freedom has been fruitful in compounds containing the pnictogens Sb or Bi, where substitution of the former with the latter is found to fundamentally influence the topology of the electronic ground state [8–11]. However, investigations of the more subtle ways in which SOC influences a material’s basic characteristics – its growth kinetics, crystal structure, or metallic transport properties – have received less attention.

In pursuit of this perspective, this work targets a class of compounds known for a

* falson@caltech.edu

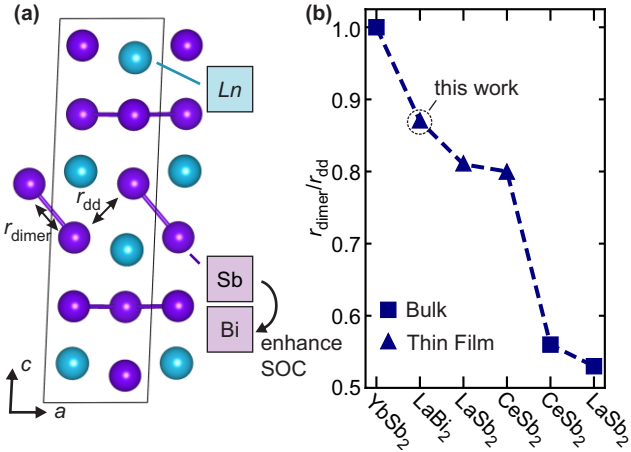


FIG. 1. (a) Yb-monoclinic structure observed in thin films of the light rare-earth dipnictides. Substitution of the Sb anion with Bi is expected to enhance SOC due to the larger atomic mass. (b) Degree of spacer-layer Pn dimerization in several reported compounds [6], including the results presented in this work.

chemistry-sensitive competition between structural and electronic phases – the $LnPn_2$ (Ln = lanthanide element, Pn = Sb, Bi) family of layered square-net intermetallics. A schematic representation of this structural class is shown in Fig. 1a. Variations in the oxidation state of the Ln cation influence the stacking configuration of the corrugated Ln - Pn and quasi-planar Pn layers, resulting in distinct orthorhombic or monoclinic structure types which can be parametrized via the dimerization of Pn atoms within the corrugated layer (Fig. 1b) [12]. In addition to the chemistry of the Ln site, previous work on thin films of LaSb_2 and CeSb_2 discovered an instability with respect to Sb deficiency, establishing UHV thin-film growth techniques as a way to access new polymorphs with modified electronic properties [13, 14].

With a desire to study the impacts of anion-tunable SOC in this subset of materials, this report builds upon the aforementioned work on $(\text{La, Ce})\text{Sb}_2$ [13, 14] and focuses on thin-films of LaBi_2 synthesized via molecular beam epitaxy (MBE). The substitution of Sb with Bi in this work acts to amplify SOC and significantly influences the thin-film growth mode and conductivity. We find LaBi_2 to exhibit superior metallic behavior compared to LaSb_2 , although not due to an intuition based on augmented hopping amplitudes, but rather due to suppressed phonon scattering at elevated temperatures arising from the spin-orbit induced shifting of electronic states.

II. METHODS

A. Experimental Details

We have synthesized LaBi_2 thin films using an MBE system with a base pressure of 10^{-10} mbar on MgO (001) substrates which are laser-annealed as in Refs. [13–15] to optimize surface quality before growth. La and Bi fluxes were provided from conventional effusion cells with a large Bi/La beam-flux ratio (10~15) while the substrate was heated with a standard SiC heating coil. A growth rate-controlling La flux of about 7.5×10^{-9} mbar established a growth rate of approximately 0.034 \AA/s . Due to the known air-sensitivity of the compound, all films were finalized with an amorphous Ge capping layer of approximately 5 nm thickness deposited *in-situ* at room temperature and then stored in a N_2 -atmosphere glovebox. Even with these precautions, film degradation was observed within a few hours of air exposure (See Fig. S1 of the Supplemental Material [16]).

Structural properties of the films were characterized by X-ray diffraction (XRD) (SmartLab, Rigaku). Electrical data above 2 K were collected using a Quantum Design Dynacool PPMS with a 14 T superconducting magnet. The film was cut into an approximately square-shaped piece ($\approx 1 - 2$ mm side lengths) and wire-bonded into a four-point van der Pauw geometry with Al wire. Magnetoresistance and Hall resistivity were extracted by symmetrizing the computed ρ_{xx} or anti-symmetrizing the diagonal R_{yx} Van der Pauw channel, respectively, with respect to a magnetic field applied perpendicular to the film. Measurements of the superconducting transition below 1 K were gathered using a Leiden dilution refrigerator equipped with a two-axis vector magnet (9 and 3 T). The sample is fashioned into a rectangular ($\sim 1 \times 2$ mm) piece and bonded with a linear four-point bond geometry.

B. Theoretical Details

Density functional theory (DFT) calculations were performed using the Quantum ESPRESSO package [17]. The exchange-correlation interaction was described by the PBEsol functional [18], chosen for its accuracy in reproducing experimental lattice constants. Ion-electron interactions were treated using norm-conserving pseudopotentials [19]. The electronic wavefunctions were expanded in a plane-wave basis set with a kinetic energy cutoff of 100 Ry. To account for the partial occupancies of electronic states near the chemical

potential, we employed the Methfessel-Paxton smearing technique [20] with a broadening width of 0.01 Ry. The Brillouin zone integration was performed using the Monkhorst-Pack scheme [21], where we used a \mathbf{k} -grid of $8 \times 6 \times 6$ for the bulk calculations. For the slab models used in the surface energy calculations, an $8 \times 8 \times 1$ \mathbf{k} -grid was adopted, and a vacuum layer of approximately 15 Å was inserted to avoid spurious interactions between periodic images. All atomic structures were fully relaxed until the residual forces on each atom converged to less than 1.0×10^{-6} Ry/ a_0 .

The electronic structure and electron-phonon coupling calculations were performed using interface with Wannier90 [22] and EPW code [23]. The elements of the electron-phonon matrix were initially computed on coarse grids of $8 \times 6 \times 6$ \mathbf{k} -points and $4 \times 2 \times 2$ \mathbf{q} -points, which were then interpolated onto dense \mathbf{k} - and \mathbf{q} -grid of $30 \times 20 \times 20$ for electron and phonon wavevectors, respectively. The electron group velocities were calculated using Wannier90, while the conductivity and scattering rates were obtained using EPW based on the Boltzmann Transport Equation (BTE). Integration for conductivity and scattering rates was performed using adaptive smearing within an energy window of ± 0.5 eV around the Fermi level, ensuring sufficient coverage of the active transport states.

III. PROPERTIES OF LaBi_2 THIN FILMS

We begin by canvassing the history of LaBi_2 . Previous reports have provided conflicting characterizations of the crystal structure, ranging from trigonal to orthorhombic crystal classes, and the structure is absent in the Inorganic Crystal Structure Database (ICSD) [24–26]. This is presumably due in part to the extreme air sensitivity of the compound. Nevertheless, a layered compound reminiscent of LaSb_2 is typically assumed to describe the structure. Despite being an excellent metal, LaBi_2 remains the only member of the La-Bi alloy system without reported ambient-pressure superconductivity besides the rock-salt structured LaBi [24]. Meanwhile, in addition to the modified dimerization illustrated in Fig. 1b, thin films of both LaSb_2 [13] and CeSb_2 [14] display a unique structure-type characterized by a monoclinic shear, in contrast to bulk orthorhombic crystals. The unique insights that thin films have provided into the delicate structural properties of this class of materials have motivated our efforts to synthesize LaBi_2 and characterize its structure.

Figure 2 illustrates our entry point for producing high-quality, single-phase films. Four

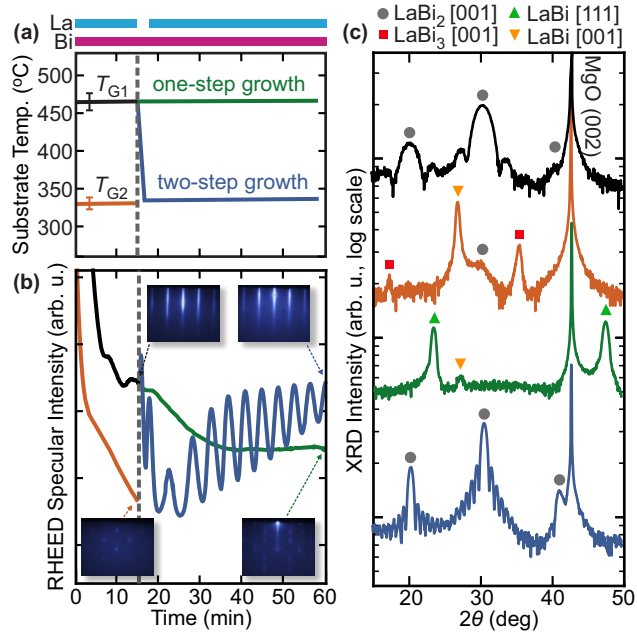


FIG. 2. (a) Schematic view of growth approaches attempted for LaBi₂ synthesis, showing substrate temperature over time with the provided elemental fluxes represented by colored bars at the top. (b) Intensity of specular RHEED diffraction over the course of growth for each approach. Inset: RHEED patterns at selected stages of growth. (c) Snippet of the X-ray diffraction (XRD) $\theta/2\theta$ diffraction pattern resulting from each growth approach.

representative films correspond to distinct sequences of substrate temperatures (labeled $T_{G1} \approx 450 - 465$ °C and $T_{G2} \approx 325 - 335$ °C, Fig. 2a) with fixed La and Bi beam fluxes. We focus first on the initial 15 minutes of growth. At the higher temperature T_{G1} (black), the film quickly develops a streaky RHEED pattern with oscillating intensity (Fig. 2b), indicating a flat crystal coating the MgO surface in a layer-by-layer fashion. Out-of-plane XRD shows reflections from the (001) LaBi₂ lattice planes without impurity phases, where we have assumed the same diffraction conditions as observed in bulk crystals (Fig. 2c) [27, 28]. This higher T_G , however, is found to be unsuitable for prolonged growth; the RHEED pattern gradually dims and degrades into a spottier series of streaks, as shown in Fig. 2b. XRD confirms this to represent a complete decomposition of the LaBi₂ film into (111)-oriented LaBi, as shown in the green trace in Fig. 2c. This can be understood in terms of the continuous thermal desorption of Bi from the substrate; due to its low melting point and high vapor pressure, lower growth temperatures are typically employed in the initial stages

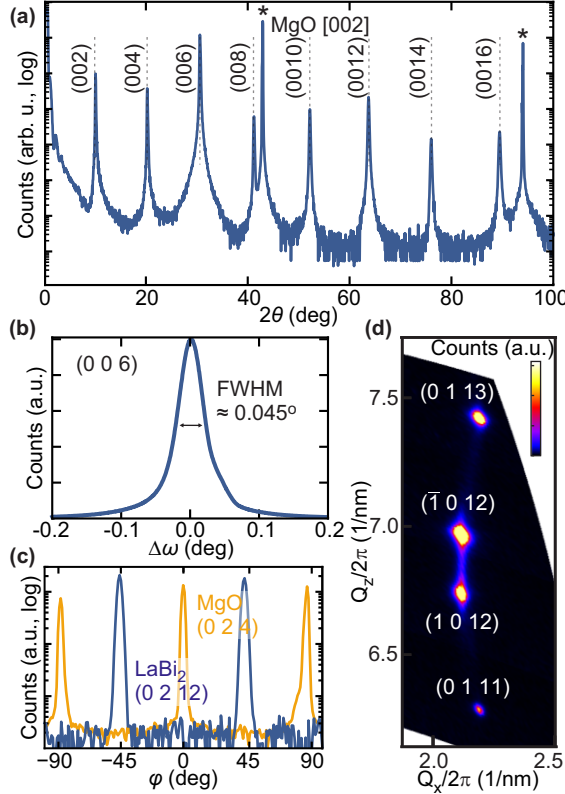


FIG. 3. (a) $\theta/2\theta$ diffraction pattern from a 75 nm film produced by the optimized two-step growth approach. (b) Rocking curve of the (006) peak. (c) Azimuthal φ -scan of an asymmetric diffraction peak showing a $[100]_{\text{LaBi}_2} \parallel [110]_{\text{MgO}}$ register with the MgO substrate. (d) Reciprocal space map along the $h = 1$ rod, showing finite splitting along Q_z consistent with the Yb-mono structure.

of growth for thin films of Bi-based compounds to ensure proper Bi adhesion, followed by a higher T_G deposition to improve film crystallinity [29–33].

To test this approach, we begin with a lower temperature T_{G2} as illustrated by the orange traces in Figs. 2a–2c. Here, RHEED dims rapidly and displays diffuse features even at the 15 minute mark, with XRD reflecting a mixed-phase film composed of LaBi[002], LaBi₂, and peaks associated with AuCu₃-structured LaBi₃ [34]. Some combination of limited surface migration energy and excessive Bi incorporation at low temperatures likely contributes to this behavior, driving the system towards multiple competing phases. The approach to realizing single-phase films is therefore a two-step process; starting with a high- T_G buffer to obtain a phase pure template layer followed by an extended low- T_G growth period (blue), the RHEED pattern persists and oscillates in intensity, and the resulting film is found to

be phase-pure LaBi_2 with sharp (001) Bragg peaks and pronounced Laue fringes. This modified two-step procedure demonstrates the complex thermodynamics at play in the thin-film growth of intermetallic phases containing volatile species.

TABLE I. Calculated relative total energies, lattice constants, and angles of the Sm-type and Yb-mono bulk phases of LaBi_2 without (with) SOC. SG denotes the space group. Experimental values reported in the literature and obtained in this work are also included for comparison.

System		SG	ΔE (meV/La)	a (Å)	b (Å)	c (Å)	α (°)	β (°)	γ (°)
Without SOC	Sm-type	64	110.21	4.575	4.575	18.275	90.00	90.00	90.74
	Yb-mono	12	0.000	4.649	4.588	17.457	90.00	87.11	90.00
With SOC	Sm-type	64	70.06	4.598	4.598	18.121	90.00	90.00	90.69
	Yb-mono	12	0.000	4.689	4.573	17.411	90.00	87.38	90.00
Experimental	Bulk exp.[25]			4.74	4.56	17.51			
	This work			4.73	4.57	17.50	90.0	86.85	90.0

Figure 3 summarizes the structural analysis of a 75 nm film grown via the optimized two-step procedure. Sharp, high-intensity Bragg peaks from the {001} LaBi_2 lattice planes in the XRD $\theta/2\theta$ scan (Fig. 3a) indicate both considerable crystal quality and the strong X-ray scattering expected from heavy Bi ions. The spacing of the Bragg peaks corresponds to an out-of-plane lattice constant $c \approx 17.5$ Å. Rocking curve analysis of the (006) diffraction condition (Fig. 3b) gives a FWHM $\approx 0.045^\circ$, indicating a uniform orientation of lattice planes throughout the film. φ -scans of both the LaBi_2 film and MgO substrate in Fig. 3c demonstrate a $[100]_{\text{LaBi}_2} \parallel [110]_{\text{MgO}}$ epitaxial register without 45° -rotated domains.

Figure 3d shows asymmetric reciprocal space mapping (RSM) taken along the $h = 1$ rod (See Fig. S4 of the Supplemental Material for extended RSM [16]). As observed in epitaxial films of LnSb_2 , we observe a finite splitting of the $(\pm 1 0 12)$ peak along Q_z associated with an out-of-plane tilt of the \vec{d}^* reciprocal lattice vector. This implies a monoclinic structure for the LaBi_2 thin films [13], in contrast to the orthorhombic space group previously assumed in bulk crystal studies. The diffraction observed in RSM can be accurately indexed with in-plane lattice constants $a \approx 4.73$ Å, $b \approx 4.57$ Å, and a monoclinic tilt of $\beta \approx 86.9^\circ$ applied to one of three possible space groups (No. 12 $A2/m$, No. 5 $A2$, No. 8 Am) [35]. While a definitive space group assignment based on XRD alone is not possible, supporting

density functional theory (DFT) calculations of the thermodynamic stability of potential stacking configurations point towards the Yb-monoclinic structure as lower in energy than the competing Sm-type structure reported in bulk LaSb_2 crystals [13]. The energy per La atom, the calculated lattice parameters both with and without SOC, and thin-film and bulk crystal experimental lattice parameters [25, 26] are reported in Table I. The close agreement between these results suggests that the MBE-grown films stabilize in the same stacking configuration as bulk samples grown in Bi flux, which is in contrast to the case of LaSb_2 [13]. The lattice parameters appear consistent with the Yb-monoclinic phase to within $\sim 1\%$. We therefore suspect that bulk studies have up to now misindexed monoclinic LaBi_2 as an orthorhombic system. Due to the restrictions imposed by the samples' air sensitivity, we have been unsuccessful in directly imaging the crystal structure using electron microscopy.

A summary of magnetotransport measurements on the 75 nm thick LaBi_2 film is presented in Fig. 4. The temperature-dependent sheet resistivity (Fig. 4a) shows metallic behavior with a RRR ($\rho_{xx}(300 \text{ K})/\rho_{xx}(2 \text{ K})$) of over 32. The anti-symmetrized Hall resistivity and symmetrized magneto-resistance ratio (MRR) are presented in Fig. 4b-c. The non-linear ρ_{yx} suggests at least two carrier types with a dominant hole-like species. The nearly linear, non-saturating MRR surpasses 100% at 14 T.

Previous reports of LaBi_2 transport properties were restricted to temperatures above the millikelvin regime. In Fig. 4d, we present resistance measurements down to $T = 20 \text{ mK}$ where a sharp transition to a zero-resistance superconducting state is observed at about 550 mK at zero field. Suppression of this transition via a magnetic field applied perpendicular to the film confirms it as a transition into a superconducting ground state. Our phase-pure XRD analysis and UHV growth environment with persistent Bi desorption make it unlikely that this superconducting transition is a result of an extrinsic impurity phase; furthermore, reports of extrinsic superconductivity due to filamentary or thin-film Bi impurities in Bi-based compounds tend to occur at much higher temperature scales on the order of 1–2 K [36]. We therefore conclude that this represents the first observation of intrinsic superconductivity in LaBi_2 at ambient pressure. The superconducting coherence length is obtained by fitting the temperature-dependent critical field $H_{c2}(T)$ to the single-gap Ginzburg-Landau model,

$$H_{c2}^\perp(T) = \left(\frac{\Phi_0}{2\pi\xi_{ab}^2} \right) \left(1 - \left(\frac{T}{T_c} \right)^2 \right). \quad (1)$$

We find $\xi_{ab} \approx 221 \text{ nm}$. Based upon an estimate of the mean free path of 300 nm using

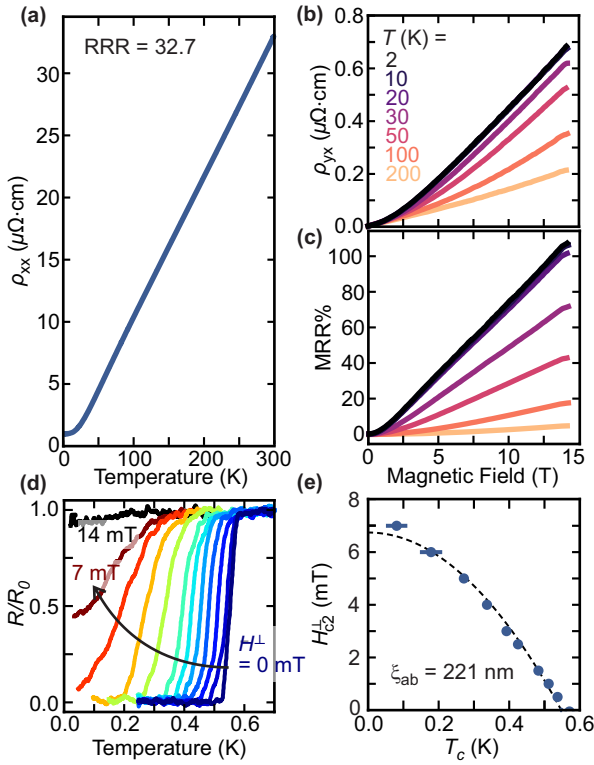


FIG. 4. (a) Temperature-dependent sheet resistivity ρ_{xx} of a 75 nm film down to 2 K. (b) Hall resistivity ρ_{yx} and (c) symmetrized magnetoresistance ratio (MRR) under an out-of-plane field at a series of temperatures. (d) Superconducting transitions below 1 K plotted as the temperature-dependent ratio of resistance to normal-state resistance R_0 , for a series of perpendicular magnetic fields. (e) Upper critical field H_{c2}^{\perp} (defined at $R = 0.5R_0$) versus temperature. Fit to the single-gap Ginzberg-Landau formula shown as dashed line.

the multicarrier Drude framework, we can infer that the films are likely clean-limit superconductors at this thickness.

IV. COMPARISON OF LaPn_2 , $Pn = \text{Sb, Bi}$

Despite the crystallographic similarities, there are notable differences between the growth dynamics and electronic properties of LaSb_2 and LaBi_2 , which will be the focus of the remainder of this manuscript. One notable difference is the strong RHEED oscillations observed during growth, as shown in Fig. 2, which are not observed in LaSb_2 for any experimental condition. As RHEED oscillations are typically associated with a layer-by-layer growth

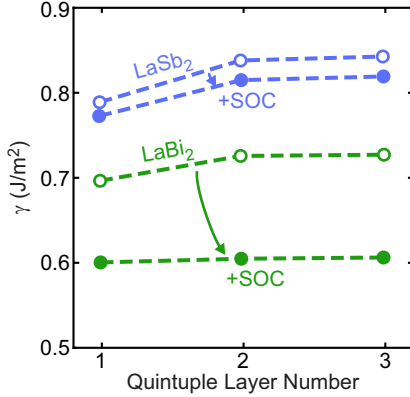


FIG. 5. Calculated surface energy γ as a function of the number of quintuple layers for LaSb_2 (blue) and LaBi_2 (green). The filled (open) circles represent the results obtained with (without) spin-orbit coupling (SOC).

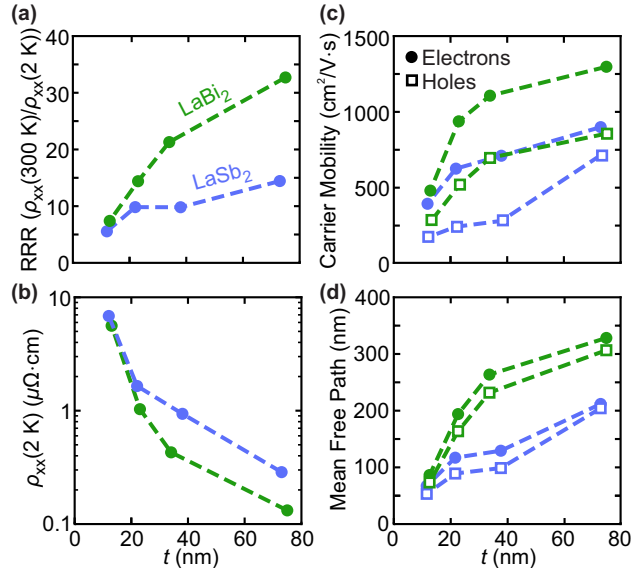


FIG. 6. Comparison of experimental transport characteristics between LaSb_2 and LaBi_2 for several film thicknesses. (a) RRR and (b) base-temperature residual resistivity, the latter plotted on a log scale. Approximate (c) carrier mobility and (d) mean free path as estimated by fits of magnetotransport data to the two-carrier Drude model.

mode, this contrast points to a stark difference in the surface energies of the (001) lattice planes. To substantiate this analysis, density functional theory (DFT) calculations were performed to evaluate the surface energies of the LaSb- or LaBi-terminated corrugated lay-

ers as a function of quintuple layer (QL) thickness, where two QLs stacked along \vec{c} comprise one conventional unit cell (See Fig. S5 of the Supplemental Material [16]). The results of these calculations are shown in Fig. 5. The surface energies are determined from [37, 38]

$$\gamma = \frac{E_s - nE_{\text{bulk}}}{2A}, \quad (2)$$

where E_s is the total energy of the slab, E_{bulk} the bulk energy per atom, n the number of atoms in the slab, and A the surface area. The surface energies are found to converge rapidly at two QL, and two features stand out; LaBi_2 has a smaller surface energy for all thicknesses than LaSb_2 , and the inclusion of SOC significantly lowers these values, especially for LaBi_2 .

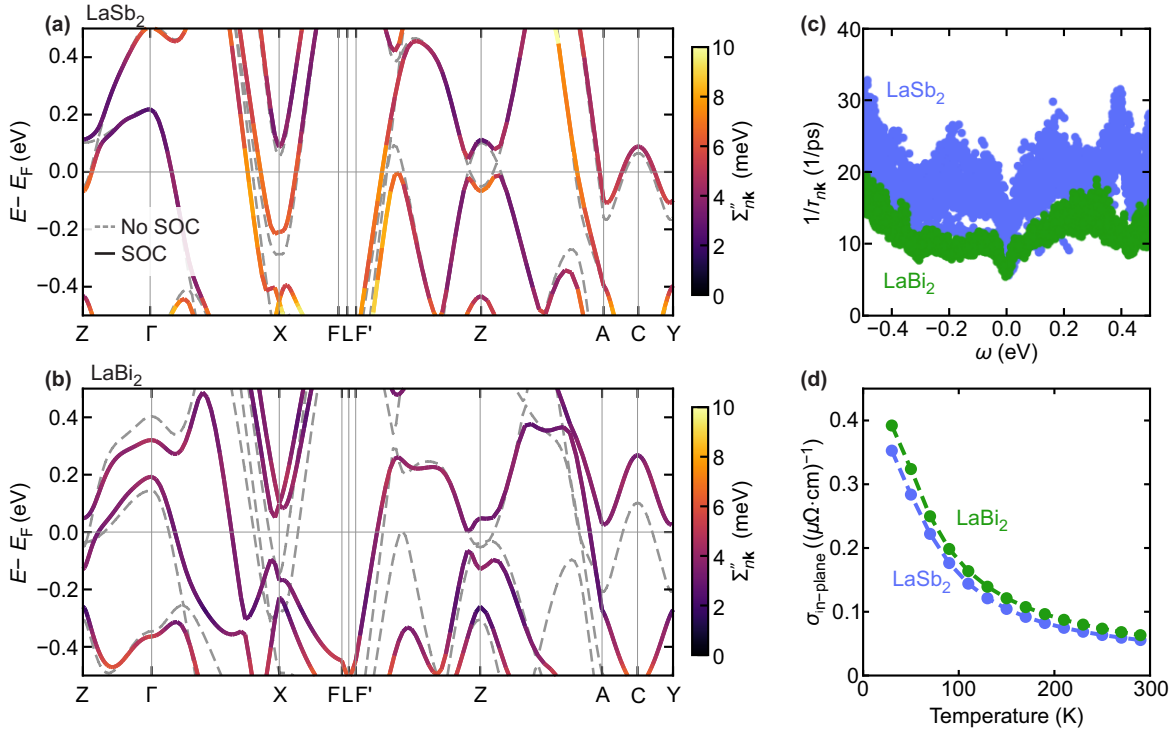


FIG. 7. (a) LaSb_2 and (b) LaBi_2 band structures with (solid) and without (dashed) SOC. In the case of SOC, colors denote the band- and \mathbf{k} -dependent $\Sigma''_{n\mathbf{k}}$ which is proportional to the scattering rate. (c) Calculated scattering rate for different band indices n and \mathbf{k} points, and (d) temperature-dependent in-plane conductivity, $\sigma_{\text{in-plane}} = (\sigma_{xx} + \sigma_{yy})/2$ for LaBi_2 (green) and LaSb_2 (blue), respectively.

The transport properties of LaSb_2 and LaBi_2 are compared in Fig. 6 across several film thicknesses. The RRR (Fig. 6a) and low- T residual resistivity (Fig. 6b) values are directly

obtained from electrical measurements, whereas the carrier mobilities (Fig. 6c) and mean free paths (Fig. 6d) are extracted from multicarrier Drude fits as described in the Fig. S5 of the Supplemental Material [16]. LaBi₂ is observed to be more conducting than LaSb₂ regardless of the metric used. While this may be intuitively attributed to an increased hopping integral for the enlarged Bi orbitals, our proceeding analysis of the band structure and phonon scattering rates provides an alternative insight into this behavior.

In order to understand the underlying origin of the transport properties of the two compounds, we have carried out *ab initio* calculations of the electrical conductivity tensor elements, $\sigma_{\alpha\beta}$, for the bulk phase, employing the self-energy relaxation time approximation (SERTA) [23, 39–41],

$$\sigma_{\alpha\beta} = en_e\mu_{e,\alpha\beta} = -\frac{e^2}{\Omega} \sum_{n \in \text{CB}} \int_{\Omega_{\text{BZ}} \in \text{CB}} d\mathbf{k} \frac{\partial f_{n\mathbf{k}}^0}{\partial \varepsilon_{n\mathbf{k}}} v_{n\mathbf{k},\alpha} v_{n\mathbf{k},\beta} \tau_{n\mathbf{k}}^0, \quad (3)$$

where α, β denote Cartesian coordinates, n_e the electron carrier concentration, e the electron charge, $\mu_{e,\alpha\beta}$ the electron mobility tensor component, Ω and Ω_{BZ} the volumes of the unit cell and the first Brillouin zone, respectively, $\varepsilon_{n\mathbf{k}}$ the single-particle electron eigenvalue of band index n and wave vector \mathbf{k} , $f_{n\mathbf{k}}^0$ the equilibrium Fermi-Dirac distribution function, $v_{n\mathbf{k},\alpha} = \hbar^{-1} \partial \varepsilon_{n\mathbf{k}} / \partial k_\alpha$ the α component of the group velocity, the sum runs over band indices n within the conduction band (CB), and $\tau_{n\mathbf{k}}^0$ is the band- and \mathbf{k} -dependent electron-phonon (el-ph) relaxation time.

The scattering rate, $1/\tau_{n\mathbf{k}}^0$, defined as the inverse of the relaxation time can be directly calculated from the imaginary part of the el-ph self-energy [23, 40, 41],

$$\begin{aligned} 1/\tau_{n\mathbf{k}}^0(\omega, T) &= 2\Sigma''_{n\mathbf{k}}(\omega, T) = \frac{2\pi}{\hbar} \sum_{m\nu} \int_{BZ} \frac{d\mathbf{q}}{\Omega_{\text{BZ}}} |g_{mn,\nu}(\mathbf{k}, \mathbf{q})|^2 \\ &\times \left\{ [n_{\mathbf{q}\nu}(T) + f_{m\mathbf{k}+\mathbf{q}}(T)] \delta(\omega - (\varepsilon_{m\mathbf{k}+\mathbf{q}} - \varepsilon_F) + \omega_{\mathbf{q}\nu}) \right. \\ &\left. + [n_{\mathbf{q}\nu}(T) + 1 - f_{m\mathbf{k}+\mathbf{q}}(T)] \delta(\omega - (\varepsilon_{m\mathbf{k}+\mathbf{q}} - \varepsilon_F) - \omega_{\mathbf{q}\nu}) \right\}. \end{aligned} \quad (4)$$

where ω is the energy of the electron, T the temperature, $\omega_{\mathbf{q}\nu}$ the frequency, $n_{\mathbf{q}\nu}(T)$ the occupation (using Bose-Einstein statistics) of the phonon mode ν at wave vector \mathbf{q} , and $g_{mn,\nu}(\mathbf{k}, \mathbf{q})$ the electron-phonon matrix element between Kohn-Sham states (n, \mathbf{k}) and $(m, \mathbf{k} + \mathbf{q})$ interacting with a phonon mode with wave vector \mathbf{q} and band index ν . The temperature dependence of the scattering rate arises from the electron and phonon occupations at finite temperatures, while electron-phonon matrix is calculated at $T = 0$.

Figures 7a and 7b show the band structures of LaSb_2 and LaBi_2 , respectively, calculated with and without SOC. In both panels, the band structures are color-coded according to the imaginary part of the self-energy (i.e., inverse of the relaxation time). While LaSb_2 exhibits relatively large scattering rates in some parts of the bands, LaBi_2 shows overall smaller scattering rates throughout the Brillouin zone.

To quantitatively corroborate the different scattering rates (and hence electron-phonon interactions) between the two systems, the scattering rate, $1/\tau_{n\mathbf{k}}^0(\omega, T = 0)$, as a function of the chemical potential is collected over all band indices and sampled \mathbf{k} -points and displayed as a scatter plot, as shown in Fig. 7c. This clearly demonstrates (i) substantially larger scattering rates in LaSb_2 compared to those in LaBi_2 over a wide range of chemical potential (and hence charge doping) and (ii) a wider distribution of scattering rates in LaSb_2 , indicating the sensitivity of the relaxation time to both band index and the electron momentum. We attribute this difference in scattering rates between LaSb_2 and LaBi_2 to significant relativistic effects in LaBi_2 .

The calculated temperature-dependent in-plane conductivity, $\sigma_{\text{in-plane}} = (\sigma_{xx} + \sigma_{yy})/2$, is shown in Fig. 7d for LaSb_2 and LaBi_2 . As these calculations neglect the impact of static disorder, they cannot be compared directly to our experimentally obtained values. Nevertheless, they show that the relatively larger conductivity of LaBi_2 over the entire temperature range considered arises from the lower scattering rates in LaBi_2 compared to LaSb_2 , rather than from differences in their relative group velocities (See Fig. S8 of the Supplemental Material [16]). In summary, we attribute both key differences between the isostructural compounds LaBi_2 and LaSb_2 to the enhanced SOC in LaBi_2 and its impact on the electronic structure. Our calculations show that the relativistic correction fundamentally alters the Fermi surface by shifting bands relative to the Fermi energy at high-symmetry points in the Brillouin zone. Consequently, the resulting energy landscape exhibits weaker phonon scattering and lower surface energy, which lead to more metallic transport and enhanced layer-by-layer growth in LaBi_2 compared to LaSb_2 .

V. CONCLUSION

We have reported the thin-film synthesis and the structural and electrical characterization of LaBi_2 . Our structural analysis agrees well with bulk-reported lattice parameters but

reveals a monoclinic structure, similar to thin films of LaSb_2 [13], suggesting that previous bulk studies misindexed the compound. We have also demonstrated ambient-pressure superconductivity with $T_c \sim 0.55$ K. Beyond these findings, this work elucidates the subtle role of SOC in influencing both thin-film growth dynamics and metallicity. Compared to LaSb_2 , SOC in LaBi_2 lowers the (001) surface energy and suppresses carrier scattering near the Fermi energy, resulting in layer-by-layer growth and superior electrical conductivity.

VI. ACKNOWLEDGMENTS

This material is based upon work supported by the National Science Foundation Graduate Research Fellowship under Grant No. 2139433. We acknowledge funding provided by the Gordon and Betty Moore Foundation’s EPiQS Initiative (Grant number GBMF10638), the Institute for Quantum Information and Matter, a NSF Physics Frontiers Center (NSF Grant PHY-2317110). The work at CSUN was supported by the NSF-PREP CSUN/Caltech-IQIM Partnership (Grant No. 2216774). The calculations were carried out in an Advanced Beowulf Cluster funded by the NSF grant number DMR-2406524. S.-H.J. was supported by Basic Science Research Institute Fund (NRF grant number RS-2021-NR060139).

- [1] M. Z. Hasan and C. L. Kane, *Rev. Mod. Phys.* **82**, 3045 (2010).
- [2] X.-L. Qi and S.-C. Zhang, *Rev. Mod. Phys.* **83**, 1057 (2011).
- [3] R. A. Klemm, A. Luther, and M. R. Beasley, *Phys. Rev. B* **12**, 877 (1975).
- [4] B. T. Zhou, N. F. Q. Yuan, H.-L. Jiang, and K. T. Law, *Phys. Rev. B* **93**, 180501 (2016).
- [5] S. J. Youn, M. H. Fischer, S. H. Rhim, M. Sigrist, and D. F. Agterberg, *Phys. Rev. B* **85**, 220505 (2012).
- [6] R. Wang and H. Steinfink, *Inorg. Chem.* **6**, 1685 (1967).
- [7] S. C. De la Barrera, M. R. Sinko, D. P. Gopalan, N. Sivadas, K. L. Seyler, K. Watanabe, T. Taniguchi, A. W. Tseng, X. Xu, D. Xiao, and B. M. Hunt, *Nat. Commun.* **9**, 1427 (2018).
- [8] J. Liu and D. Vanderbilt, *Phys. Rev. B* **88**, 224202 (2013).
- [9] Y. H. Liu, C. W. Chong, W. C. Chen, J. C. A. Huang, C.-M. Cheng, K.-D. Tsuei, Z. Li, H. Qiu, and V. V. Marchenko, [arXiv:1611.08395](https://arxiv.org/abs/1611.08395) (2016).
- [10] X. He, H. Li, L. Chen, and K. Wu, *Sci. Rep.* **5**, 8830 (2015).
- [11] D. A. Glazkova, D. A. Estyunin, I. I. Klimovskikh, A. A. Rybkina, I. A. Golovchanskiy, O. E. Tereshchenko, K. A. Kokh, I. V. Shchetinin, V. A. Golyashov, and A. M. Shikin, *JETP Lett.* **116**, 817 (2022).
- [12] G. A. Papoian and R. Hoffmann, *Angew. Chem. Int. Ed.* **39**, 2408 (2000).
- [13] A. Llanos, G. Campisi, V. Show, J. Kim, R. Dorrian, S. Salmani-Rezaie, N. Kiouassis, and J. Falson, *Nano Lett.* **24**, 8518 (2024).
- [14] R. Dorrian, J. Kim, M. Ohno, A. Llanos, V. Show, N. Kiouassis, and J. Falson, *Nano Lett.* **25**, 11427 (2025).
- [15] A. Llanos, S. Salmani-Rezaie, J. Kim, N. Kiouassis, D. A. Muller, and J. Falson, *Cryst. Growth Des.* **24**, 115 (2024).
- [16] See Supplementary Material [URL] for detailed characterization, which includes Ref. [13].
- [17] P. Giannozzi, S. Baroni, N. Bonini, M. Calandra, R. Car, C. Cavazzoni, D. Ceresoli, G. L. Chiarotti, M. Cococcioni, I. Dabo, A. D. Corso, S. d. Gironcoli, S. Fabris, G. Fratesi, R. Gebauer, U. Gerstmann, C. Gougoussis, A. Kokalj, M. Lazzeri, L. Martin-Samos, N. Marzari, F. Mauri, R. Mazzarello, S. Paolini, A. Pasquarello, L. Paulatto, C. Sbraccia, S. Scandolo, G. Sclauzero, A. P. Seitsonen, A. Smogunov, P. Umari, and R. M. Wentzcovitch,

J. Condens. Matter Phys. **21**, 395502 (2009).

[18] J. P. Perdew, A. Ruzsinszky, G. I. Csonka, O. A. Vydrov, G. E. Scuseria, L. A. Constantin, X. Zhou, and K. Burke, Phys. Rev. Lett. **100**, 136406 (2008).

[19] D. R. Hamann, Phys. Rev. B **88**, 085117 (2013).

[20] M. Methfessel and A. T. Paxton, Phys. Rev. B **40**, 3616 (1989).

[21] H. J. Monkhorst and J. D. Pack, Phys. Rev. B **13**, 5188 (1976).

[22] A. A. Mostofi, J. R. Yates, Y.-S. Lee, I. Souza, D. Vanderbilt, and N. Marzari, Comput. Phys. Commun. **178**, 685 (2008).

[23] S. Poncé, E. Margine, C. Verdi, and F. Giustino, Comput. Phys. Commun. **209**, 116 (2016).

[24] F. Hulliger and H. R. Ott, J. Less-Common Met. **55**, 103 (1977).

[25] K. Nomura, H. Hayakawa, and S. Ono, J. Less-Common Met. **52**, 259 (1977).

[26] C. Petrovic, S. L. Bud'ko, and P. C. Canfield, J. Magn. Magn. Mater. **247**, 270 (2002).

[27] K. Yoshihara, J. B. Taylor, L. D. Calvert, and J. G. Despault, J. Less-Common Met. **41**, 329 (1975).

[28] W. Zhou, C. Q. Xu, B. Li, R. Sankar, F. M. Zhang, B. Qian, C. Cao, J. H. Dai, J. Lu, W. X. Jiang, D. Qian, and X. Xu, Phys. Rev. B **97**, 195120 (2018).

[29] H. D. Li, Z. Y. Wang, X. Kan, X. Guo, H. T. He, Z. Wang, J. N. Wang, T. L. Wong, N. Wang, and M. H. Xie, New J. Phys. **12**, 103038 (2010).

[30] T. Fan, M. Tobah, T. Shirokura, N. Huynh Duy Khang, and P. Nam Hai, Jpn. J. Appl. Phys. **59**, 063001 (2020).

[31] N. Bansal, Y. S. Kim, E. Edrey, M. Brahlek, Y. Horibe, K. Iida, M. Tanimura, G.-H. Li, T. Feng, H.-D. Lee, T. Gustafsson, E. Andrei, and S. Oh, Thin Solid Films **520**, 224 (2011).

[32] K. Ueda, Y. Hadate, K. Suzuki, and H. Asano, Thin Solid Films **713**, 138361 (2020).

[33] W. K. Loke, K. H. Tan, S. Wicaksono, and S. F. Yoon, Mater. Sci. Eng. B **294**, 116533 (2023).

[34] T. Kinjo, S. Kajino, T. Nishio, K. Kawashima, Y. Yanagi, I. Hase, T. Yanagisawa, S. Ishida, H. Kito, N. Takeshita, K. Oka, H. Eisaki, Y. Yoshida, and A. Iyo, Supercond. Sci. Technol. **29**, 03LT02 (2016).

[35] D. H. Flack (International Union for Crystallography, 2016) Chap. 1.6, pp. 114–128.

[36] L. Xiang, E. Gati, K. Neilson, S. L. Bud'ko, and P. C. Canfield, Phys. Rev. Mater. **3**, 095006 (2019).

[37] W. Sun and G. Ceder, Surf. Sci. **617**, 53 (2013).

- [38] J. C. Boettger, *Phys. Rev. B* **49**, 16798 (1994).
- [39] J. M. Ziman, *Electrons and Phonons: The Theory of Transport Phenomena in Solids* (Oxford University Press, Oxford, New York, 2001).
- [40] F. Giustino, *Rev. Mod. Phys.* **89**, 015003 (2017).
- [41] S. Poncé, E. R. Margine, and F. Giustino, *Phys. Rev. B* **97**, 121201 (2018).

Multi-carrier fitting: The estimated carrier mobilities reported in the main text were obtained from fits of the magnetoresistance and Hall resistivity (Fig. S6) to the two-carrier Drude formulas,

$$\rho_{xx} = \frac{1}{e} \frac{(p\mu_h + n\mu_e) + (p\mu_e + n\mu_h)\mu_h\mu_e B^2}{(p\mu_h + n\mu_e)^2 + (p - e)^2\mu_h^2\mu_e^2 B^2} \quad (5)$$

$$\rho_{yx} = \frac{B}{e} \frac{(p\mu_h^2 - n\mu_e^2) + (p - n)^2\mu_h^2\mu_e^2 B^2}{(p\mu_h + n\mu_e)^2 + (p - e)^2\mu_h^2\mu_e^2 B^2} \quad (6)$$

where n (p) and μ_e (μ_h) are the carrier density and mobility of electron-like (hole-like) carriers, respectively, B is the applied magnetic field, and e is the electron charge. Fits are performed to both $\rho_{xx}(B)$ and $\rho_{yx}(B)$ simultaneously, with the additional constraint that the zero-field conductivity agrees with $\sigma_{xx}(B = 0) = e(n\mu_e + p\mu_h)$.

Orbital-projected band structures: Figure S7 presents the orbital-projected band structures of LaBi₂ with and without spin-orbit coupling (SOC). Significant SOC due to the heavy mass of bismuth induces hybridization of the La-*d* and Bi-*p* orbitals, modifying the overall shape of the band structure. Consequently, electron and hole pockets disappear in the vicinity of the zone boundaries (specifically, near X and C points), thus significantly altering the intrinsic electron-phonon scattering conditions.

Electronic group velocities: The magnitudes of the group velocities, $|v_g|$, projected onto the band structures of LaSb₂ and LaBi₂ are shown in Fig. S8. LaBi₂ exhibits smaller group velocities than LaSb₂ due to the band modification induced by SOC, specifically the gap opening near the X point and the lifting of electron/hole pockets along the A – C – Y path. This confirms that the higher conductivity of LaBi₂ originates from the relaxation time τ_{nk}^0 , which compensates for the relatively small group velocity $|v_g|$.

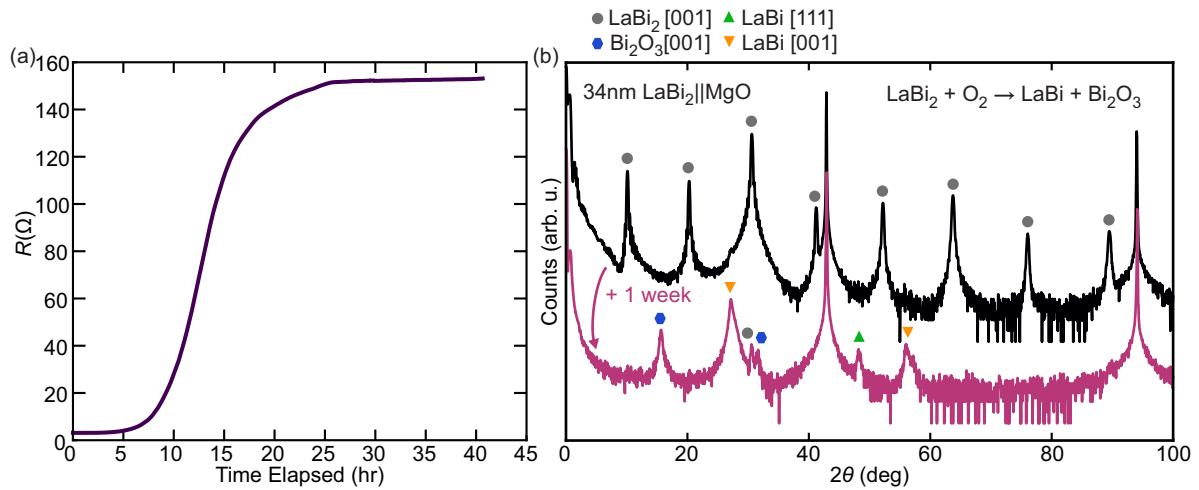


FIG. S1. Degradation of a Ge-capped LaBi_2 film through air exposure. (a) Four-point resistance of a $\sim 0.5 \times 1\text{cm}$ sample versus time in air. Resistance slowly rises during the first few hours of exposure, then degradation rapidly accelerates and saturates after roughly 24 hours. (b) $\theta/2\theta$ scans showing phase composition of a film before and after complete degradation. LaBi_2 peaks are diminished in place of multiply-oriented LaBi and Bi_2O_3 .

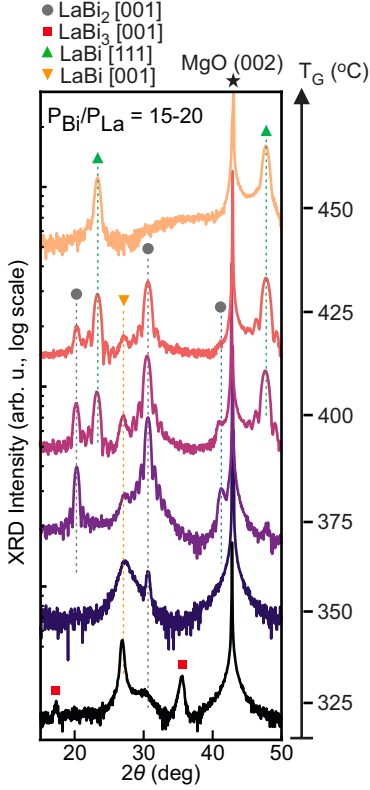


FIG. S2. $\theta/2\theta$ diffraction patterns resulting from single-step growth at fixed substrate temperature T_G for 1 hour. Maximum $T_G = 450^\circ\text{C}$ and minimum $T_G = 325^\circ\text{C}$ reported in the main text where excessive Bi desorption and limited migration energy at the substrate surface, respectively, result in dominant impurity phases. A small window around 375°C shows the most phase-purity of the series albeit with a noticeable LaBi impurity still present. Thus a two-step growth procedure is a necessity to produce single-phase LaBi_2 thin films of appreciable thickness.

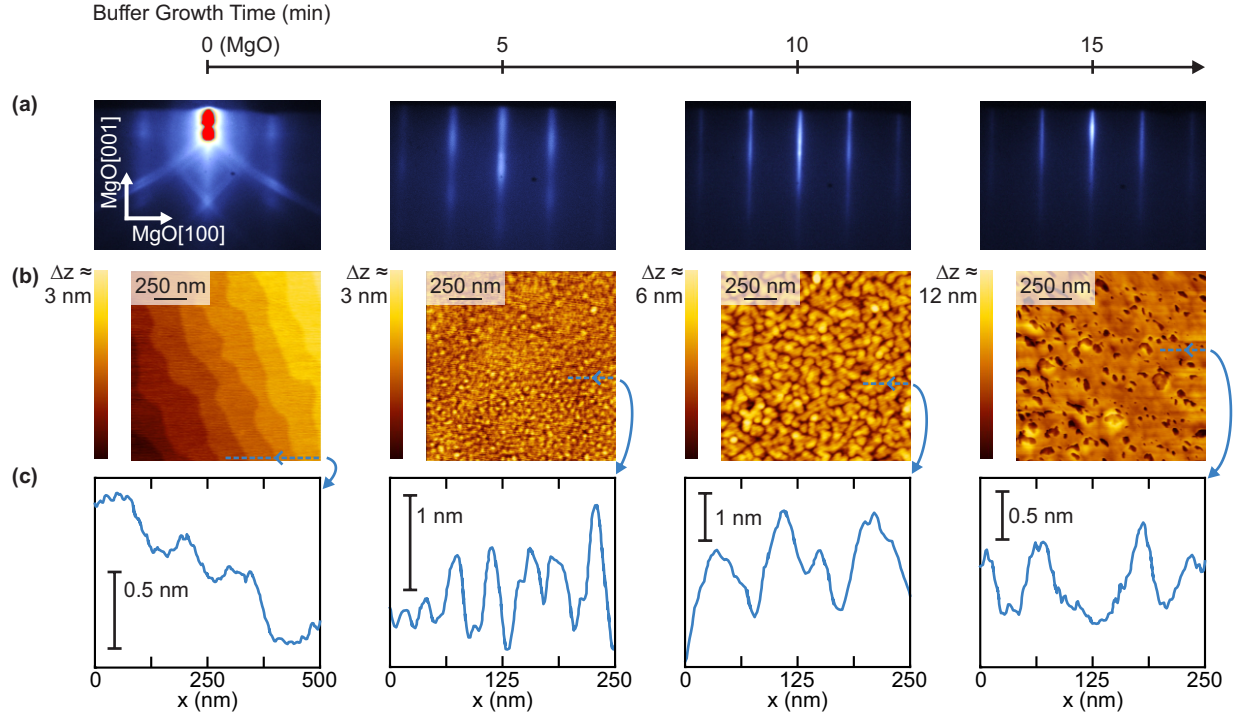


FIG. S3. Progression of buffer layer growth at $T_G \approx 450\text{-}475^\circ\text{C}$ viewed by (a) *in-situ* RHEED and (b) atomic force microscopy (AFM, performed in an N_2 -environment glovebox). To better represent the morphology of the samples, representative line-cuts are shown in (c). The step-terraced MgO substrate becomes decorated with $\sim 1 \text{ nm}$ tall islands in the first 5 minutes of growth, which gradually merge as the film wets the substrate surface. By 15 minutes of growth the film becomes flat and contiguous besides some residual pits where the film has yet to merge.

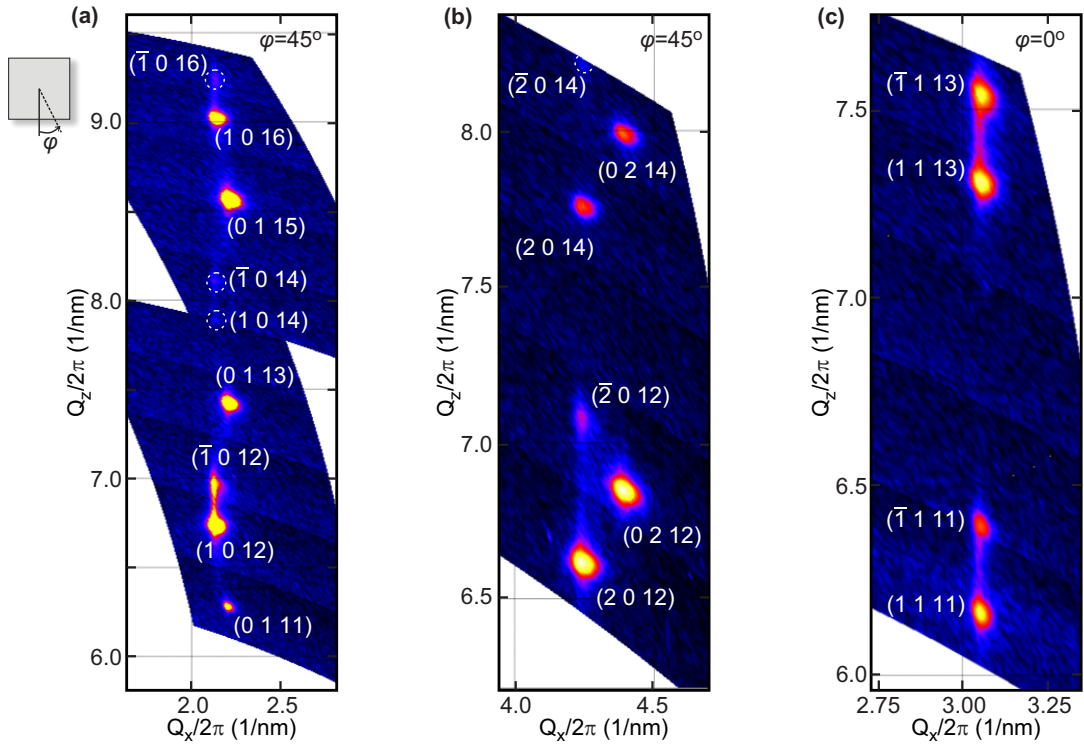


FIG. S4. Extended reciprocal space mapping along the (a) $h = 1$, (b) $h = 2$, and (c) $h = k = 1$ rods. Splitting along Q_z is observed for all diffractions with non-zero h . These three scans along with the $\theta/2\theta$ pattern indexed in the main text allow full identification of the structure's extinction coefficients; $\ell = 2n$ for (00ℓ) ; $k + \ell = 2n$ for $(0k\ell)$; $\ell = 2n$ for $(h0\ell)$; $k + \ell = 2n$ for $(hk\ell)$. This is consistent with three possible monoclinic space groups (SG 5, 8, and 12), between which space group 12 is identified via first-principles DFT calculations.

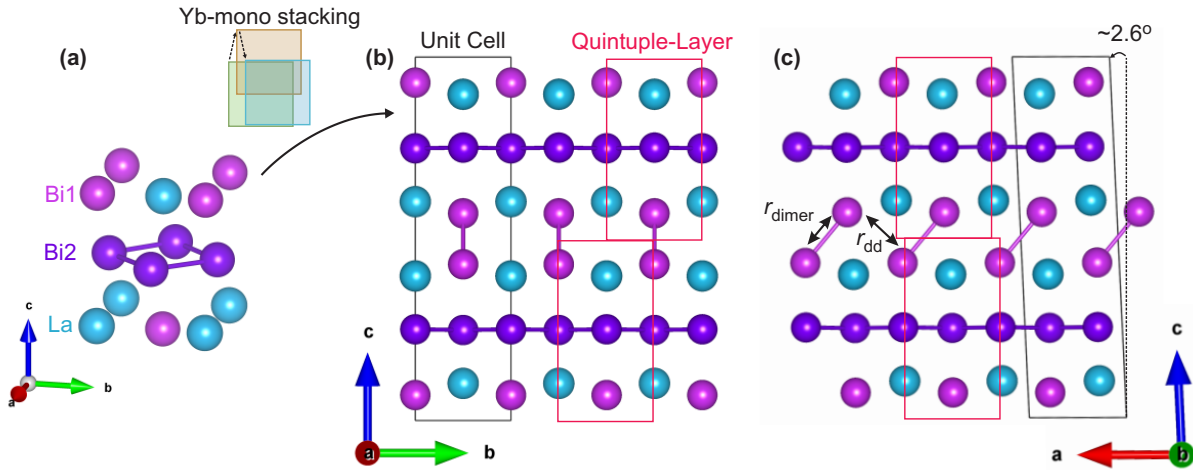


FIG. S5. Yb-monoclinic structure of the LaBi_2 in terms of the quintuple-layer construction. (a) A single quintuple-layer block contains one distinct La and two distinct Bi sites. The Yb-mono structure is obtained by a staggered stacking configuration of these blocks [13]. The resulting structure is shown along the (b) \vec{a} and (c) \vec{b} crystallographic directions.

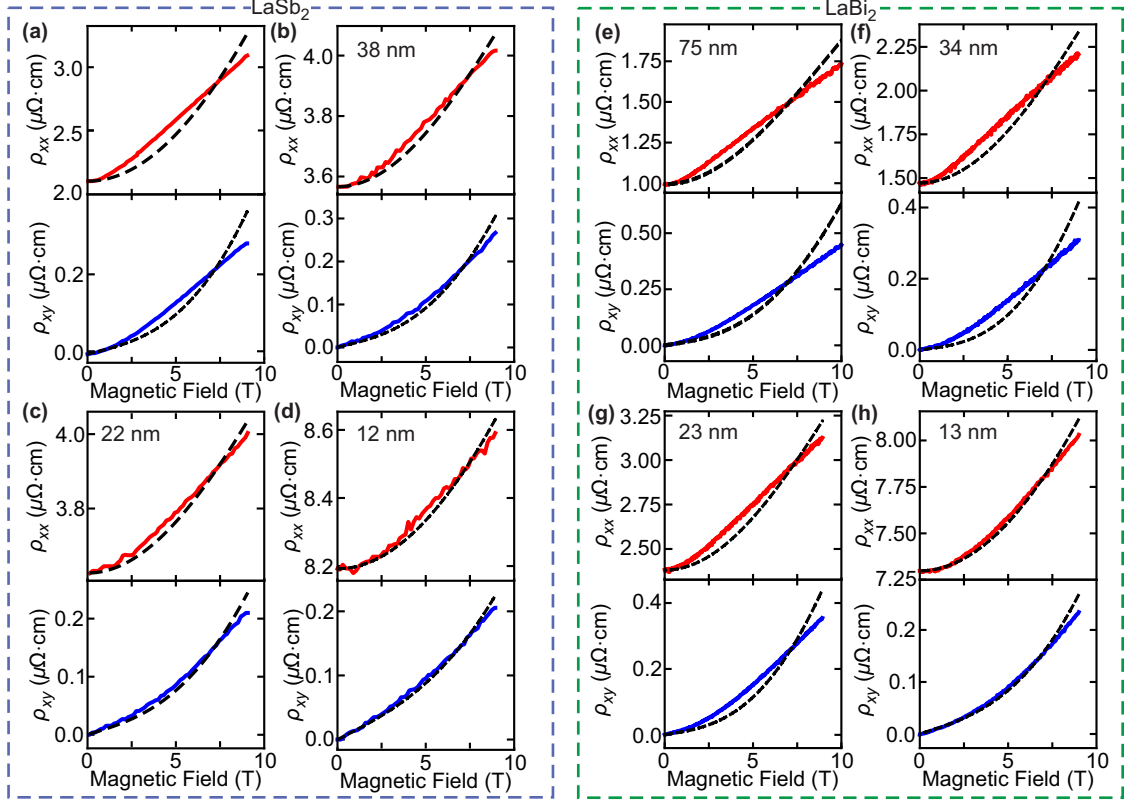


FIG. S6. Fitting of the two-carrier Drude model to longitudinal magnetoresistance and hall resistivity data for (a-d) LaSb_2 and (e-h) LaBi_2 , for four representative film thicknesses. Significant deviations from the model are apparent in the thicker films primarily due to the non-quadratic behavior of the magnetoresistance. However, these deviations are apparent in both compounds so direct comparison of the fit parameters between both series is acceptable for the purpose of this study.

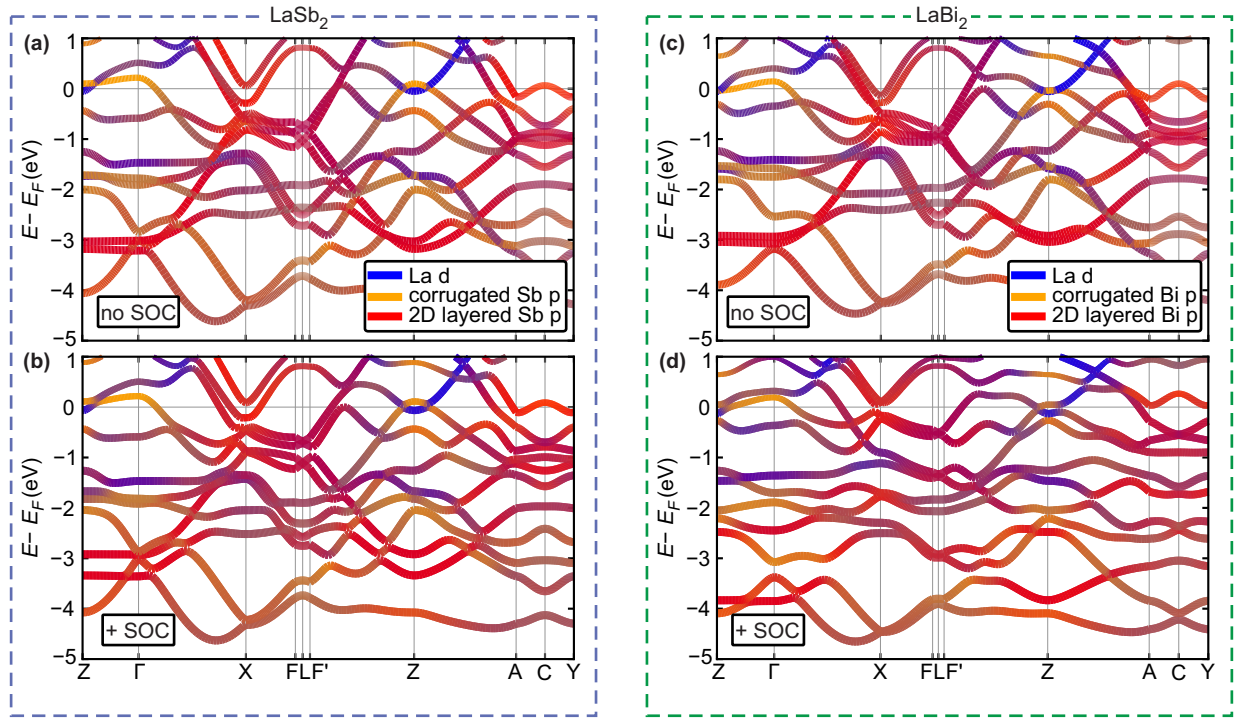


FIG. S7. The orbital-projected band structures of (a, b) LaSb_2 and (c, d) LaBi_2 without and with SOC.

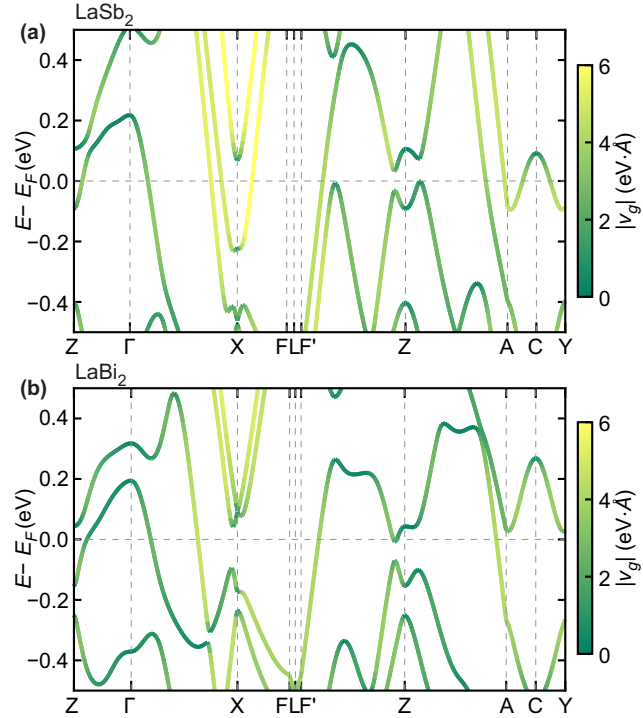


FIG. S8. The band structures with SOC projected by electronic group velocities of (a) LaSb₂ and (b) LaBi₂.